Journal of Materials Chemistry A

PAPER

View Article Online
View Journal | View Issue

Cite this: J. Mater. Chem. A, 2015, 3, 8380

Synergistic effect of a *r*-GO/PANI nanocomposite electrode based air working ionic actuator with a large actuation stroke and long-term durability†

Qing Liu,[ab] Luqi Liu,*[a] Ke Xie,[a] Yuena Meng,[ab] Haiping Wu,[ab] Guorui Wang,[a] Zhaohe Dai,[ab] Zhixiang Wei[a] and Zhong Zhang*[a]

Received 27th January 2015
Accepted 9th March 2015

DOI: 10.1039/c5ta00669d

www.rsc.org/MaterialsA

Actuators can directly convert various types of energy into mechanical motions. In this work, we constructed a novel air working ionic actuator by sandwiching sulfuric acid–poly(vinyl alcohol) (H_2SO_4–PVA) gel electrolyte between two pieces of reduced graphene oxide/polyaniline (*r*-GO/PANI) nanocomposite film based electrode, in which the PANI nanoparticles were uniformly decorated onto the *r*-GO sheet surfaces through an *in situ* polymerization method. A combination of the supramechanical properties, electrical conductivity, large surface area of the individual graphene sheets and excellent electrochemical properties of the PANI component results in the composite electrode having good mechanical properties and a high electrochemical capacitance. Later tests indicated that the actuator could be stimulated under a low driving voltage (≤0.5 V) without trade-off actuator strokes, and showed excellent long-term actuation durability. Under a 0.5 V operating voltage, the actuation strain of the *r*-GO/PANI actuator could reach 0.327%, corresponding to a 30 MPa generated stress. We attribute the excellent actuation performance to the synergistic effect of the *r*-GO sheets and the PANI component.

Introduction

Actuators that can directly convert various energies to mechanical energy have shown great potential in many fields such as artificial muscles, robots, sensors, *etc.*[1–5] Among all the electrically stimulated actuators that have been explored, air operable ionic actuators have been extensively studied in recent decades for their impressive actuation performances under relatively lower driving voltages.[6–8] Generally, an air working ionic actuator is constructed of an ionic conductive electrolyte layer laminated by two pieces of electrically conductive electrode membranes. During the actuation process, ion migration caused by the applied electric field induces a volume difference of the anode and cathode layers, and the actuator strip will bend forth and back under an alternative potential. Even though traditional ionic polymer–metal composite (IPMC) type actuators have been commercially available in recent years, the intrinsic weaknesses of metal electrode layers (*e.g.* silver, gold, and platinum), including low flexibility, cracking of the metal electrodes during the application process, and high manufacturing costs, have greatly limited their wide application in the smart materials field.[6,9] Thus, it is a great challenge to explore novel electrode materials with higher flexibilities and excellent electromechanical stabilities for the next-generation of air working ionic actuators.

Nanostructured carbon materials, such as one-dimensional (1D) carbon nanotubes (CNTs) and two-dimensional (2D) graphene, have attracted extensive attention in the smart materials field due to their excellent electrical conductivities, outstanding mechanical properties, large specific surface areas and thermal/chemical stabilities.[10,11] Baughman first reported a single wall carbon nanotube (SWCNT) based ionic actuator that could work in an electrolyte solution, demonstrating the potential applications of nanostructured carbon materials in ionic actuators.[12] Since then, CNTs have been explored to satisfy various requirements of ionic actuator electrodes, and plenty of works have proved the excellent actuation performances of CNT electrode based air working actuators. For instance, Aida *et al.* have proved the excellent electromechanical stability of a CNT gel based actuator, and only a 20% decrease in the actuator stroke was observed after 15 hours of actuation.[8] It should be noted, however, that the force generation was limited due to the low modulus of the gel electrodes.[13]

Having intrinsically structural similarity with both CNTs and graphene building blocks, graphene based paper materials show higher tensile mechanical properties compared to CNT buckypaper.[11] Thus, enhancements in output stress and power

[a]National Center for Nanoscience and Technology, Beijing, P. R. China, 100190. E-mail: zhong.zhang@nanoctr.cn; liulq@nanoctr.cn; Fax: +86-10-6265-6765; Tel: +86-10-8254-5586/+86-10-8254-5587

[b]University of Chinese Academy of Science, 100049, Beijing, China

† Electronic supplementary information (ESI) available. See DOI: 10.1039/c5ta00669d

density are expected when graphene papers are utilized as actuator electrodes. Experimentally, different from CNTs prepared by a chemical vapour deposition (CVD) method, graphene sheets can be easily prepared on a large scale by chemical reduction of graphene oxide (GO), which would extremely facilitate the electrode fabrication.[14,15] Theoretical calculations have predicted that the quantum-mechanical strain of graphene in the basal plane direction could reach 0.2%, while the electrostatic double-layer strain could reach 1% for charge injection, which are much higher than the values for CNTs.[16,17] Therefore, ionic actuators with large actuation strokes and high generated stress would be obtained when graphene papers are utilized as electrodes. Previous work has demonstrated the potential applications of graphene film based electrodes in liquid-type ionic actuators.[18,19] It is worth noting, however, that the dense stacking nature of graphene sheets hinders ion migration, and severely deteriorates the actuation performance of graphene based ionic actuators, particularly under air conditions. Thus, it is crucially important to design graphene based electrodes with loosely packed architectures, which could exhibit large actuation strokes, high stress generation, and good stability.

Earlier work has proven that incorporating a second component, such as CNTs or nanoparticles, is a promising approach to prevent restacking of graphene sheets.[20–23] For instance, the incorporated CNTs can greatly restrain the restacking behaviour of individual graphene or GO sheets, and facilitate the diffusion of electrolytes across electrode layers. Consequently, improvements in both electrochemical and actuation properties were obtained in graphene/CNT hybrid electrode based actuators.[21,22] Chen *et al.* reported that under a 2 V, 0.01 Hz square wave potential, the actuation stroke could reach about 2 mm for a graphene/CNT actuator under ambient conditions.[21] They also demonstrated that through hybridizing RGO and Ag nanoparticles, the electrochemical stability of the Ag-based electrochemical actuators was significantly improved.[23] Besides the CNTs and nanoparticles mentioned above, electrochemical active materials, such as conducting polymers (CPs), have also been employed as spacers to act as obstacles to prevent the restacking of graphene or GO sheets.[24–29] Although earlier work has pointed out that CPs exhibited poor stability during the charge/discharge process due to the configuration change, recent work reported by Wei *et al.* has proven that PANI–GO nanocomposite electrodes display excellent electrochemical stability over thousands of consecutive cycles due to a synergistic effect of the PANI nanowire array and GO sheets.[24] Consequently, enhancements in the actuation stroke, stress generation, and electromechanical stability are expected when graphene/CP composites are utilized as the actuator electrode.

In this work, PANI was used as an interlayer spacer to fabricate a *r*-GO/PANI nanocomposite electrode due to its high specific capacitance, low cost, and facial fabrication procedure. PANI nanoparticles were directly decorated onto the *r*-GO sheet surfaces through *in situ* chemical polymerization in the presence of aniline monomer, and a vacuum-assisted filtration method was employed to fabricate the macroscopic free-standing *r*-GO/PANI hybrid electrode. As expected, the presence of PANI nanoparticles could effectively inhibit the restacking of graphene sheets, and then facilitate ion migration and accumulation in the electrode layers. Acid cross-linked PVA based gel (H_2SO_4–PVA gel) was selected as the electrolyte layer due to its high ionic conductivity.[30,31] Actuation tests indicated that the actuation could be stimulated by an extra low voltage (0.1 V), which is lower than other graphene-based air working ionic actuators reported in the literature.[21–23] Under a 0.5 V, 0.01 Hz square wave voltage, the bending displacement of the actuator could reach 4.300 mm, corresponding to a strain of 0.327%, which is larger than that of other graphene based air working actuators driven at higher voltages.[21,23] We attribute the large actuation stroke of the *r*-GO/PANI actuator to a synergistic effect of the electric double-layer capacitor (EDLC) behaviour of the *r*-GO component and the pseudocapacitance of the PANI component. Our study will guide the design and preparation of nanostructured carbon material based ionic actuators with high actuation strokes, large generated stress and long-term durability at low driving voltages.

Experimental section

Preparation of *r*-GO and the *r*-GO/PANI nanocomposite film electrodes

GO was synthesized from purified natural graphite by Hummers' method according to previous work.[32] For the GO reduction, hydroiodic acid (HI) was used, referring to Cheng's work.[15] Specifically, 100 ml of GO solution (with a concentration of 1 mg ml^{-1}) was first heated to 95 ± 5 °C, then 10 ml of HI was added and the mixture was vigorously stirred for 20 min, after which the mixture was stirred for 12 h at room temperature. The obtained *r*-GO dispersion was washed by centrifugation using deionized water (DI H_2O) and ethanol to remove the residual I^+ and I_2. Finally the product was dispersed in ethanol with a concentration of 0.6 mg ml^{-1}. The *r*-GO/PANI nanocomposite was synthesized by an *in situ* polymerization in the presence of *r*-GO and aniline monomer.[24] In a typical procedure, 50 ml of the *r*-GO dispersion was added into 200 ml of 1 M HCl solution and 95 mg of aniline monomer was added into the solution. The mixture was stirred for 1 h in an ice bath to form a uniform mixture. After that, 165 mg of oxidant, $(NH_4)_2S_2O_8$ (APS), was added into the above solution, and the mixture was stirred for another 24 h in the ice bath. The final *r*-GO/PANI precipitate was obtained and washed by centrifugation using DI H_2O, ethanol and 1 M HCl. The final dispersion was diluted to 0.6 mg ml^{-1} in DI H_2O. To prepare the *r*-GO/PANI nanocomposites with different weight ratios, the aniline monomer with weights of 47 mg and 190 mg, and APS with weights of 82 mg and 330 mg, were utilized, respectively. Elemental analysis (EA) was carried out by using a Flash EA1112 (Thermo Electron SPA) to measure the weight ratio of PANI in the nanocomposites. According to the results, the weight ratio of PANI was 50 wt%, 60 wt% and 80 wt% for *r*-GO/PANI (50/50), *r*-GO/PANI (40/60) and *r*-GO/PANI (20/80), respectively. The *r*-GO/PANI nanocomposite used for characterization was the one with 60 wt% PANI unless otherwise stated. The PANI sample was synthesized chemically using

0.15 M aniline *via* a similar procedure. The *r*-GO and *r*-GO/PANI films were prepared by vacuum filtrating a 10 ml dispersion through polytetrafluoroethylene (PTFE) and cellulose membranes (47 mm in diameter, 0.22 μm pore size). After air drying, the resulting films were peeled off from the membranes. For the PANI electrode preparation, a mixture containing 85 wt% PANI powder, 10 wt% conducting carbon black and 5 wt% PTFE (used as a binder) was mixed well and pressed into a film.

Preparation of the electrolyte layers

For the electrolyte preparation, 1 g of PVA was dissolved in 10 ml of DI H_2O, and 1 g of concentrated H_2SO_4 was added. The mixture was vigorously stirred at ~85 °C for 1 h to obtain a uniform transparent solution.[31] To obtain the electrolyte layer, 1.5 ml of H_2SO_4–PVA solution was cast into a PTFE mold with a size of 3 × 3 cm and dried at 40 °C for 4 h.

Assembly of the sandwiched actuators

The half-dried H_2SO_4–PVA gel was peeled off from the PTFE mold and two pieces of the as-prepared electrode films were pasted on the two sides of the gel and pressed under 0.7 MPa for 15 min at 40 °C. After that, the assembled actuators were aged at room temperature in air for at least 1 day to evaporate the excess H_2O in the electrolyte layer, until no weight loss was observed. The final membrane was cut into strips with a size of 2 × 25 mm for the actuation performance tests.

Material characterization and actuation performance tests

The morphology of the samples was studied using a Scanning Electron Microscope (SEM, HITACHI S-4800) and a Transmittance Electron Microscope (TEM, Tecnai G2 F20 U-TWIN). Fourier transform infrared (FTIR) spectroscopy (Spectrum One), Raman spectroscopy (using the 632.8 nm line of a He–Ne laser, equipped with a Linkam cooling cell), X-ray photoelectron spectroscopy (XPS, ESCALAB 250Xi), and X-ray diffraction (XRD, Rigaku D/max-2500) were used to examine the microstructure of the materials. The Brunauer–Emmett–Teller (BET) surface area was measured using a TriStar II 3020 analyzer. Electrochemical measurements were carried out on an EG&G Princeton Applied Research VMP3 workstation with two symmetrical electrodes and H_2SO_4–PVA gel as the electrolyte layers. The EIS measurements were carried out at 0 V by imposing a sinusoidal perturbation of 10 mV in the frequency range from 10 mHz to 100 kHz. A dynamic mechanical analyzer (TA, DMA Q800) was employed to evaluate the mechanical properties of the resulting films. The films were cut into strips with a width of 2 mm, and the gauge length was controlled to be 10.0 ± 0.5 mm. The static tensile tests were conducted in displacement ramp mode with a pre-strain of 0.01% and a ramp rate of 20 μm min^{-1}. For the actuation performance tests, the electrical power was supplied by a Tektronix arbitrary function generator (AFG3011), and the bending displacements were measured using a Keyence LK-G5001 laser displacement sensor. The vertical distance of the recorded point was 18 mm from the fixed end.

Results and discussion

The structures of the electrode materials were characterized by FTIR spectroscopy, Raman spectroscopy and XPS analysis. In the FTIR spectrum of *r*-GO (in Fig. 1a), the absorption bands at 2950 and 2865 cm^{-1} are assigned to the C–H, $(C–H)_n$ stretching vibrations. The peak around 1725 cm^{-1} originates from the stretching vibrations of C=O in the COOH functional groups, indicating the partial chemical reduction of the carboxyl groups. The presence of residual functional groups would act as nucleation sites for the formation of PANI nanoparticles during the polymerization process.[24] Similar to those for PANI, the peaks at 1595, 1487 and 1340 cm^{-1} appearing in the *r*-GO/PANI spectrum are assigned to the C=C stretching vibration of the quinonoid ring, benzenoid ring and C–N vibrations of PANI, respectively.[26] The Raman spectrum of the *r*-GO sample in Fig. 1b displays two peaks at 1352 (D band) and 1588 cm^{-1} (G band), which correspond to the *K*-point phonons of A_{1g} symmetry and the vibration of sp^2 hybridized carbon (E_{2g} phonons).[27] In the spectrum of the *r*-GO/PANI sample, several new Raman peaks are detected. The peaks at 529 and 807 cm^{-1} are assigned to the out-of-plane C–H deformation and C–H bending of the quinonoid ring, respectively.[33] The peaks at 1495 and 1595 cm^{-1} originate from C=N and C=C stretching in the quinonoid ring, respectively. Other peaks at 1166, 1223, 1340 and 1420 cm^{-1} are attributed to C–H bending of the quinonoid ring, C–N vibration of the quinonoid and benzenoid rings, stretching vibration of $C–N^{+\bullet}$, and C=N stretching of the quinonoid ring, respectively. The presence of the $C–N^{+\bullet}$ stretching vibration mode implies that PANI was doped in the nanocomposite.[34,35]

XPS characterization was used to investigate the electronic structure of the carbon based materials. For the *r*-GO/PANI nanocomposite, the C 1s spectrum could be mainly deconvoluted into five Gaussian peaks, as shown in Fig. 1c, which correspond to the C=C bond (284.5 eV), C–N bond (285.5 eV), residual C–O (286.6 eV), C=O (287.7 eV) and O–C=O (288.7 eV) functional groups, respectively. The N 1s spectrum of the *r*-GO/PANI sample (Fig. 1d) shows that three different electronic states existed in the N 1s spectrum: quinoid amine (398.8 eV), benzenoid amine (399.5 eV), and nitrogen cationic radicals ($N^{+\bullet}$) with a binding energy of 400.9 eV.[36,37] The relatively high fraction of $N^{+\bullet}$ in the N 1s core-level spectrum of the nanocomposite sample indicates a relatively high doping level of PANI, which would be beneficial for the electrochemical properties when used as electrodes.[36,37] From the XPS, FTIR and Raman results, we conclude that PANI was successfully attached onto the *r*-GO surface through dilute polymerization of the aniline monomer.

Fig. 2 shows the SEM and TEM characterization of the morphology and structure of *r*-GO, *r*-GO/PANI sheets, and the macroscopic *r*-GO, and *r*-GO/PANI papers. The *r*-GO sheets with a lateral size of several micrometers exhibit a typical crumpled and layer-like structure (Fig. 2a and b). As stated in earlier work, the *r*-GO sheets would act as excellent heterogeneous nucleation substrates for the polymerization of aniline polymer.[24–26] Fig. 2d and e show that numerous PANI nanoparticles with a size

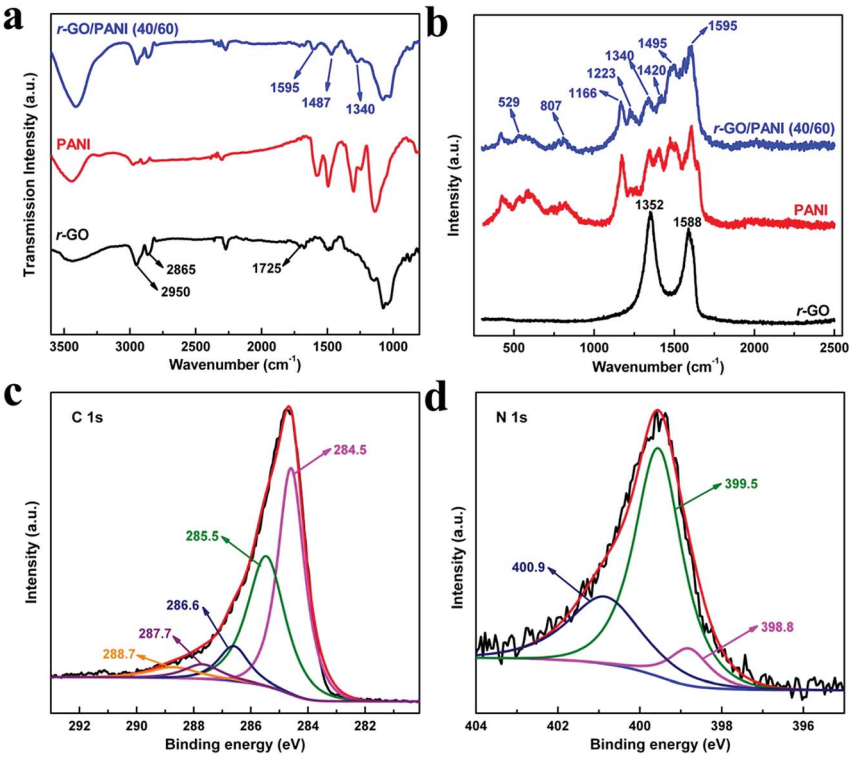

Fig. 1 (a and b) FTIR and Raman spectra of pristine *r*-GO, PANI and the *r*-GO/PANI nanocomposite; (c and d) C1 s and N1 s spectra of *r*-GO/PANI, respectively.

around 20 nm are uniformly decorated onto the surface of the graphene sheets in the *r*-GO/PANI sample. The overall morphology of the *r*-GO sheets was not affected by the presence of PANI nanoparticles, as shown in the insets of Fig. 2a and d. Since the homogenous growth of PANI was effectively restricted in the solution, there is no apparent bulk PANI material observed in the SEM and TEM images. We speculate that the presence of PANI nanoparticles on the graphene sheet surfaces would hinder the stacking of the *r*-GO sheets during the film formation process. We will discuss this later.

By using *r*-GO and *r*-GO/PANI sheets as building blocks, free-standing films were fabricated through a vacuum assisted filtration method as reported in our previous work.[32] Fig. 2c and f show that both *r*-GO and *r*-GO/PANI sheets could self-assemble into a layered structure. As expected, the *r*-GO/PANI film exhibits a relatively loosely stacked morphology compared with

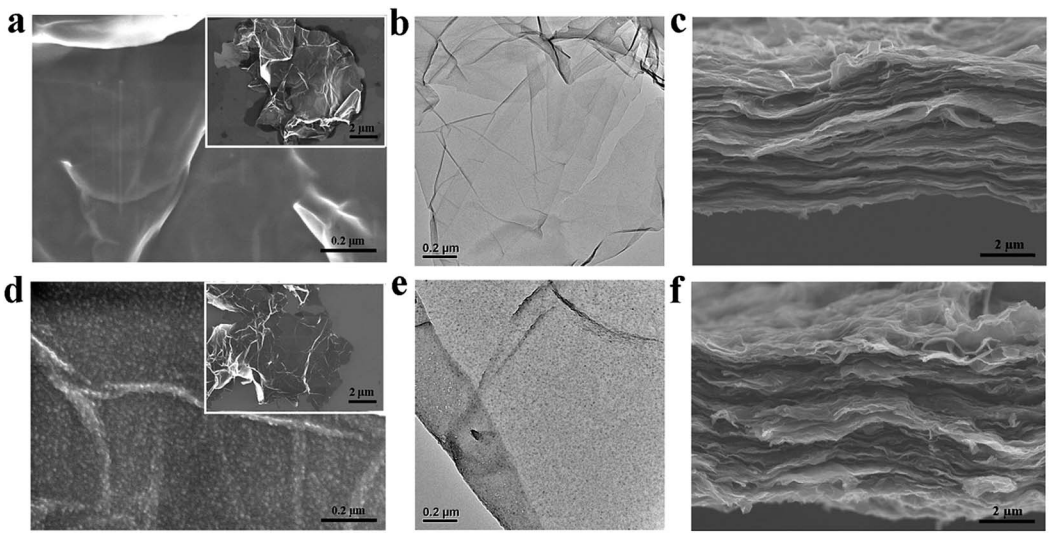

Fig. 2 SEM and TEM characterization of the *r*-GO sheets (a and b) and *r*-GO/PANI (40/60) hybrid sheets (d and e), insets are the overall morphology of the sheets; (c and f) cross-sectional views of the free-standing *r*-GO and *r*-GO/PANI films.

the densely packed *r*-GO film. To quantitatively elucidate the influence of PANI nanoparticles on the microstructure of *r*-GO sheets, XRD characterization was carried out and the results are given in Fig. 3a. The *r*-GO sheets exhibit an intense, sharp reflection peak at $2\theta = 23.24^\circ$ (assigned to the (001) reflection peak), which correlates to an interlayer spacing of 0.38 nm.[15] The neat PANI sample exhibits several broad reflection peaks around $2\theta = 15.5^\circ$, 20.7° and 25.2°, which are the characteristic Bragg diffraction peaks of PANI.[38] In the case of the *r*-GO/PANI sample, only the characteristic PANI reflection peaks at 2θ values around 15° and 20–30° are observed. The disappearance of the reflection peak for the *r*-GO sheets is attributed to the adsorption and intercalation of PANI nanoparticles, as supported by the TEM and SEM characterization shown in Fig. 2. The loosely packed feature of the graphene sheets endows the *r*-GO/PANI nanocomposite film with additional specific surface area compared with that of the compact *r*-GO film (*r*-GO sample = 3.7 $m^2\ g^{-1}$ and *r*-GO/PANI sample = 12.3 $m^2\ g^{-1}$). Consequently, an increment in the ionic transportation channels is expected, and would benefit ion migration during the electrochemical charging and discharging process.

Fig. 3b shows the electrochemical properties of the *r*-GO, PANI and *r*-GO/PANI nanocomposite examined by cyclic voltammetry (CV) with a potential window from 0 to 0.8 V and a scan speed of 10 mV s^{-1}. The specific capacitance (C) of the electrode materials can be calculated according to eqn (1):

$$C = \int \frac{IdV}{vmV} \quad (1)$$

where I, v and V are the charge/discharge current, potential scan speed and voltage range, respectively, and m is the mass of the electrode. The approximate rectangular shape of the CV curve for the *r*-GO electrode shown in Fig. 3b indicates typical EDLC behaviour, and the derived specific capacitance value is 79 F g^{-1}, which is close to the value reported by Chen *et al.*[39] As for the PANI electrode, two couples of redox peaks can be observed in the CV curve with a specific capacitance of 208 F g^{-1}, corresponding to two redox transitions of PANI (*i.e.* the leucoemeraldine/emeraldine transition and emeraldine/pernigraniline transition).[40] Compared with PANI, the peak positions of the two redox components in the *r*-GO/PANI nanocomposite electrode are very close to each other and nearly merge into one peak. A similar phenomenon was also observed in the CNT/PANI nanocomposite system.[31] The derived capacitance for *r*-GO/PANI is 207 F g^{-1}, higher than the theoretical value based on the weight ratio of the *r*-GO/PANI nanocomposite (79×40 wt% + 208×60 wt% = 156 F g^{-1}). The enhancement in specific capacitance for the nanocomposite electrode comes from the synergistic effect of the *r*-GO sheets and PANI nanoparticles. The loosely packed *r*-GO/PANI electrode exhibits a relatively larger rectangular area in the CV curve (Fig. 3b), confirming an increase in the double-layer capacitance.[40] Besides that, the presence of the PANI component in the composite electrode also contributes additional pseudocapacitance to the electrochemical properties.

Both the electrochemical properties and the mechanical properties are important factors to define the actuator performance. Fig. 3c shows the typical tensile mechanical properties of the *r*-GO and *r*-GO/PANI films. For the neat *r*-GO film, a tensile modulus and strength of 17.3 ± 0.4 GPa and 154.9 ± 11.9 MPa could be obtained. Because of the increased interlayer spacing and loosely stacked *r*-GO sheets, the modulus and strength decreased to 9.8 ± 0.2 GPa and 115.2 ± 5.0 MPa, respectively, for the *r*-GO/PANI nanocomposite. However, it should be noted that the tensile mechanical properties of the composite are still higher than the existed electrode materials, such as CNT based bucky gel (modulus is 0.2 GPa) and PANI film (modulus is 0.4 GPa).[13,41] A large actuation stroke and high stress generation are expected for the *r*-GO/PANI nanocomposite based actuator because of the large electrochemical capacitance and good mechanical properties.

The ionic-type actuators were constructed by sandwiching H_2SO_4–PVA gel with two pieces of electrode films, and the cross-sectional views of the actuators in Fig. S1† indicate that the electrode and electrolyte layers were combined together tightly. The actuation strain (ε) could be quantitatively calculated using eqn (2), where d stands for the thickness of the actuator, L is the length from the fixed end to the measured point, and δ represents the actuation displacement from the initial position to the peak position.

$$\varepsilon = \frac{2d\delta}{L^2 + \delta^2} \quad (2)$$

In this work, the values for d and L were controlled to be about 250 μm and 18 mm, respectively.

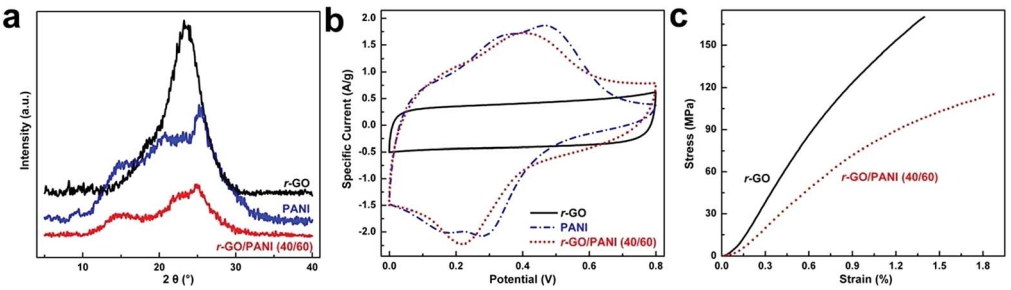

Fig. 3 (a) XRD characterization; (b) CV curves at 10 mV s^{-1} scanning speed for pristine *r*-GO, PANI and *r*-GO/PANI; (c) typical stress–strain curves for pristine *r*-GO and the *r*-GO/PANI nanocomposite.

At a given frequency, the actuation strokes of ionic actuators strongly depend on the amplitude of the driving voltage, and it is desirable to stimulate the actuator under a relatively low driving voltage.[8,42] Recently, Kim *et al.* demonstrated that, by employing self-assembled sulphonated block copolymers and ionic liquids as the electrolyte, the SWCNT actuator could work at sub-1 V conditions in air.[42] Herein, H_2SO_4–PVA gel is utilized as the electrolyte due to its high ionic conductivity and low-cost.[30,31] The actuation performances of the actuators were first investigated by applying alternating square wave voltages with various amplitudes. As shown in Fig. 4a, the displacement increases with the driving potential for all actuators. More interestingly, the actuation could be triggered under an extremely low driving voltage (0.1 V), which is about one magnitude lower than that used for graphene based ionic actuators reported in the literature.[21–23] Under a 0.1 V, 0.01 Hz square voltage, the peak-to-peak displacements of the *r*-GO, PANI and *r*-GO/PANI electrode based actuators are 0.190, 0.100 and 0.490 mm, corresponding to strains of 0.015%, 0.008% and 0.038%, respectively. It can also be seen that the deformations plateau after the voltage exceeds 0.5 V. The deformations increase to 1.010, 1.030, and 4.300 mm for the *r*-GO, PANI and *r*-GO/PANI actuators at 0.5 V, while the values are 1.050, 1.110, and 4.300 mm at 0.6 V, respectively. For the *r*-GO actuator, the deformation saturation should be related to the dense stacking nature of the sheets, which would block further ion transportation greatly. For the PANI and *r*-GO/PANI actuators, as seen from the CV curves shown in Fig. 3b, the redox reaction happens around 0.5 V, which means more ions would be transferred and accumulated at 0.5 V. If the driving voltage was further increased, there would be no significant increase in ion accumulation, and then no more bending deformation of the actuators. When the driving voltage exceeds 0.8 V, the actuation performance would deteriorate due to the overoxidation and instability of the PANI component.

The voltage–frequency-dependent actuation performances of the actuators were explored in Fig. 4b. Under a given driving voltage, the actuation stroke increases with the decrement of applied frequency. The frequency-dependent actuation strokes are attributed to variations in ion migration and accumulation, where more ions would be transported to the electrode layer at a lower frequency and lead to apparent deformation of the actuators. At a driven voltage of 0.5 V, the bending deformations of the *r*-GO, PANI and *r*-GO/PANI actuators are 1.010, 1.030, and 4.300 mm at 0.01 Hz, corresponding to strains of 0.077%, 0.079% and 0.327%, respectively. Fig. 4c shows the cyclic bending curves for the actuators under a 0.5 V, 0.01 Hz square wave voltage. For the *r*-GO based actuator, the dense stacking feature severely restricts ion migration in the electrode layers, and then the ion accumulation saturation would lead to the displacement equilibration. Different from the *r*-GO actuator, no displacement plateau region is observed for the PANI and *r*-GO/PANI actuators, which could be related to the redox reaction of the PANI component. Digital pictures showing the forth

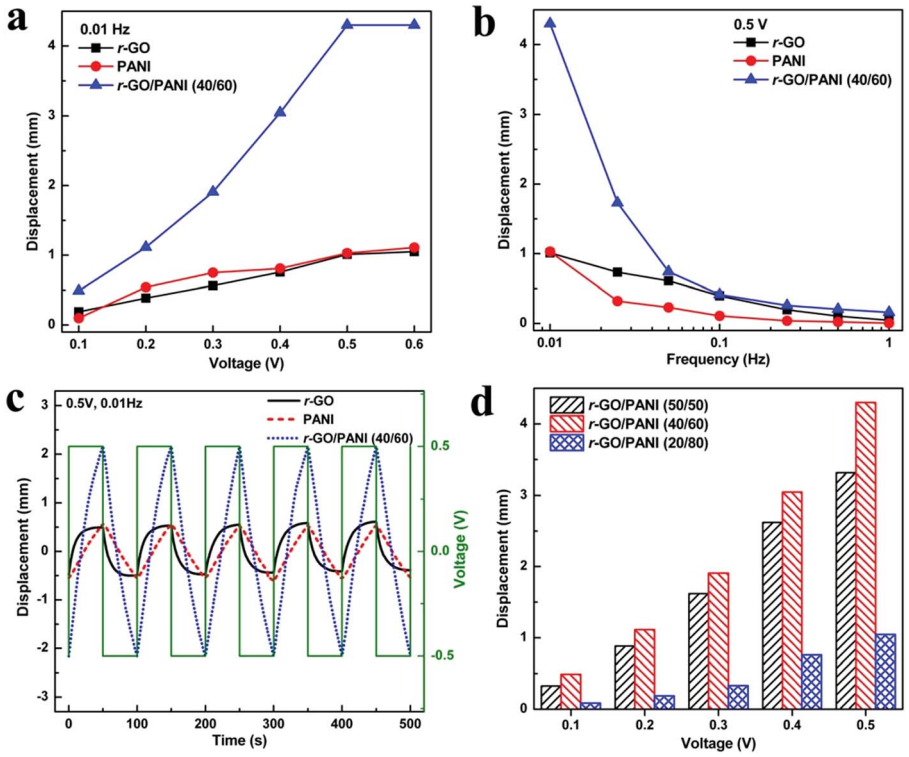

Fig. 4 (a) Actuation displacements of different actuators under various driving voltages with 0.01 Hz frequency; (b) voltage–frequency-dependent actuation performances of the actuators under a driving voltage of 0.5 V; (c) cyclic actuation curves for the *r*-GO, PANI and *r*-GO/PANI actuators under a 0.5 V, 0.01 Hz square wave voltage; (d) actuation displacements of the *r*-GO/PANI actuators with different PANI contents under various driving voltages with 0.01 Hz frequency.

and back bending deformation of the *r*-GO/PANI based actuator under a 0.5 V, 0.01 Hz voltage are shown in Fig. S2.†

To investigate the effect of the PANI content on the actuation performance, *r*-GO/PANI nanocomposites with different amounts of PANI were prepared. The weight ratios of PANI were about 50 wt%, 60 wt% and 80 wt% for *r*-GO/PANI (50/50), *r*-GO/PANI (40/60), and *r*-GO/PANI (20/80), respectively, and the capacitance values were measured to be 170, 207 and 106 F g^{-1}, respectively. This result indicates that the introduction of PANI could improve the electrochemical performance of *r*-GO, and the optimal content of PANI is 60 wt%; further increasing the PANI content would lead to the capacitance decreasing because of the nanoparticle morphology disappearance and the dense coverage on the *r*-GO sheets, as shown in Fig. S3.† Fig. 4d presents the actuation performances under various voltages at 0.01 Hz. According to the results, upon increasing the weight ratio of PANI, the deformation of the *r*-GO/PANI actuator increases remarkably. The displacement of *r*-GO/PANI (50/50) reaches 3.314 mm and the maximum (4.300 mm) is achieved for *r*-GO/PANI (40/60). The value then decreases sharply to 1.046 mm when the mass ratio of PANI is 80 wt%. It can be deduced that the bending deformation shows the same trend as the capacitance, and the *r*-GO/PANI nanocomposite with 60 wt% PANI shows the best actuation performance under same working conditions.

Electrochemical impedance spectroscopy (EIS) characterization was carried out to understand the electrochemical behaviour of the actuators as it has been proven to be a useful approach to analyze the electrochemical behaviour of air working ionic actuators.[21,22] The experiment set up is depicted in Fig. 5a, and the distances between the two electrodes were controlled to be 20 mm for all the actuators. Fig. 5b and c show the equivalent circuit used for the data analysis and the obtained Nyquist plots of the actuators. The equivalent circuit contains four main parts: R_0 stands for the actuator resistance that is mainly due to the electrolyte layer; Q_1/R_1 represents the contact impedance between the actuator electrodes and metal electrodes; Q_2/R_2 and Z_w (the Warburg impedance) indicate the ion intercalation impedance. The fitting results obtained using this equivalent circuit are given in Table S1.† According to the fitting results, the resistance R_0 is at the level of a few hundreds of Ohms. Comparatively, the contact resistance R_1 is larger than R_0, especially for PANI (3470 Ω), indicating the better electrode contact behaviour of *r*-GO (657 Ω) and *r*-GO/PANI (282 Ω). On the other hand, the diffusion ability (Z_w) for PANI and *r*-GO/PANI is relatively small compared to that for *r*-GO, but they are all at the same level, as shown in Table S1.† Additionally, after the introduction of PANI nanoparticles, the R_2 value of *r*-GO/PANI (1117 Ω) is significantly decreased compared with *r*-GO (6811 Ω), indicating the enhanced ion transfer ability of the nanocomposite electrode. More importantly, the storage ability of the interfacial ions (Q_2) in *r*-GO/PANI (324.6 mF) is significantly improved compared with *r*-GO (22.4 mF) and PANI (11.4 mF), which will contribute to the capacitive behaviour of the electrode and improve the electrochemical and electromechanical properties. Based on the EIS results, we can thus deduce that the polymerization of PANI on the *r*-GO sheet surfaces could significantly reduce the ion intercalation resistance and improve the ion storage ability of the electrode, which might cause actuation performance enhancement of the actuator consequently.

According to the electrochemical and actuation performance tests, the actuation mechanism of the actuators should be attributed to the EDLC behaviour of *r*-GO and the pseudocapacitance of PANI, as depicted in Fig. 6. When subjected to electrical stimulation, the H^+ and SO_4^{2-} ions dissociated in the gel electrolyte layer are driven to migrate and accumulate at the cathode and anode, respectively, to keep the electric field balance. For the *r*-GO electrode, the ion migration and accumulation will lead to an expansion of both the anode and cathode; however, the expansion of the anode will be more significant than the cathode due to the larger SO_4^{2-} ions compared with H^+ ions, which will then cause the sandwiched actuator to bend towards the cathode direction under air conditions. On the other hand, for PANI actuator, the ion insertion and deinsertion in the polymer backbone happens during the redox reaction process to balance the charge of the system, which then leads to dimensional changes of the polymer electrodes. Specifically, the inserted SO_4^{2-} ions in the PANI backbone would cause swelling of the polymer chains, and subsequently the anode expands, eventually leading to a convex corresponding to the positive bias.[7,43] After the introduction of PANI onto the *r*-GO sheet surfaces, because of the presence of PANI nanoparticles inside the gallery space, the synergistic effect of ion aggregation and the redox reaction induced doping will lead to a more significant bending deformation of the actuator. The increase in specific surface area and ion transportation

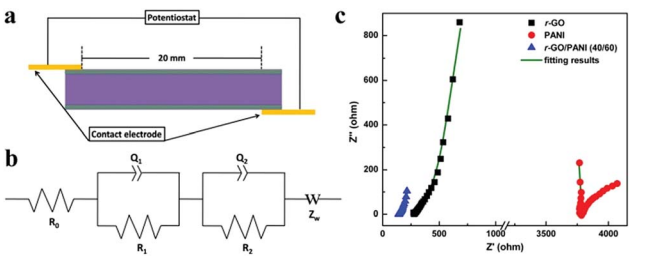

Fig. 5 (a) Illustration of the impedance characterization; (b) equivalent circuit model of the actuators; (c) Nyquist plots of the actuators.

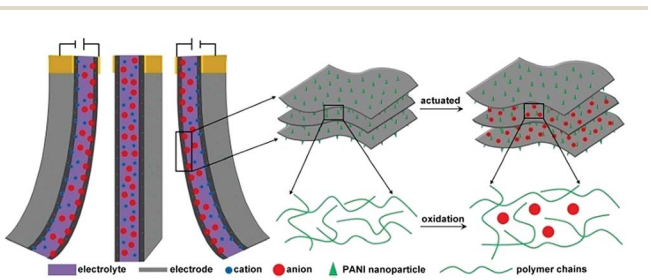

Fig. 6 Schematic drawing of the actuation deformation.

channels in the loosely packed *r*-GO/PANI nanocomposite film decrease the ion migration resistance and benefit ion transportation in the electrode, meaning more ions could be inserted and accumulated in the electrodes to consequently induce the bending deformation. Besides that, the redox reaction of PANI provides excess charge transfer to allow more ion intercalation into the electrode and improve the ion storage ability, which then contribute to the actuation performance of the composite electrode.

In comparison with graphene and/or graphene composite based air working actuators reported in the literature, the *r*-GO/PANI based actuator exhibits a higher actuation strain.[21] Specifically, with the same stimulation frequency (0.01 Hz), the actuation strains for RGO and RGO/MWCNT electrode actuators were 0.248% and 0.077%, respectively, under a 2 V potential, while the value is 0.327% for the *r*-GO/PANI actuator under a much lower voltage (0.5 V). Together with the high stiffness characteristic of the nanocomposite electrode, the generated stress of the *r*-GO/PANI electrode could reach about 30 MPa, ten times higher than that for the existing ionic actuator electrodes, such as bucky gel electrode materials (about 3 MPa).[13]

The long-term stabilities of the *r*-GO and *r*-GO/PANI actuators were investigated under 0.5 V, 0.01 Hz square wave potential, as shown in Fig. 7. During the cyclic actuation process, the *r*-GO electrode based actuator exhibited a quite stable working performance without any apparent decrease, implying the excellent durability of the *r*-GO electrode and stable ion conductivity of the H_2SO_4–PVA gel electrolyte under air conditions over long-term actuation. In comparison, the PANI actuator showed a dramatic displacement decrease by about 30% due to the swelling and shrinkage caused by degradation of the electrode material. In contrast to the poor durability of the PANI actuator, after 200 consecutive actuation cycles, the *r*-GO/PANI actuator retained ~92% of its initial displacement. The improved durability over long-term actuation of the *r*-GO/PANI actuator comes from the synergistic effect of graphene sheets and PANI nanoparticles. Graphene sheets undertake some mechanical deformation in the actuation process, which avoids further damage of the PANI component and benefits the structural stability.

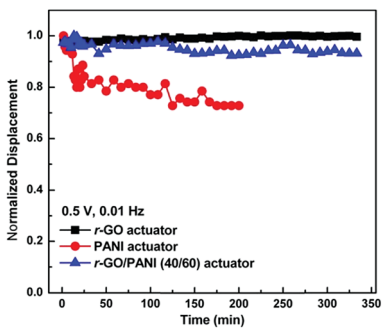

Fig. 7 Cyclic stability test of the *r*-GO, PANI and *r*-GO/PANI electrode based ionic actuators.

Conclusions

In this work, PANI nanoparticles were successfully decorated onto *r*-GO sheet surfaces through an *in situ* polymerization in the presence of aniline monomer. The attached PANI nanoparticles effectively inhibit the restacking of *r*-GO sheets during the film preparation process and improve the electrochemical properties. Electrochemical tests show that the capacitance of the *r*-GO/PANI nanocomposite increases to 207 F g^{-1}, much higher than that of the *r*-GO electrode (79 F g^{-1}). The air working ionic actuator constructed from the *r*-GO/PANI nanocomposite electrode and H_2SO_4–PVA electrolyte shows excellent low-voltage driven characteristics without trade-off actuation strokes. Specifically, under a 0.5 V square wave voltage, the bending strain could reach 0.327%. The excellent actuation performance is attributed to the synergistic effect coming from the loosely packed *r*-GO sheets and the redox reaction of the PANI component in the composite electrode, where both the ion transportation and storage ability of the electrode are significantly enhanced. Moreover, taking advantage of the excellent mechanical properties and high flexibility of the graphene component, our composite actuator performs with high stress generation and long-term durability.

Acknowledgements

This project was jointly supported by the National Key Basic Research Program of China (Grant nos 2012CB937503 and 2013CB934203) and the National Natural Science Foundation of China (Grant nos 51173030, 11225210 and 11222217).

Notes and references

1 S. Maeda, Y. Hara, T. Sakai, R. Yoshida and S. Hashimoto, *Adv. Mater.*, 2007, **19**, 3480.
2 T. Mirfakhrai, J. Madden and R. Baughman, *Mater. Today*, 2007, **10**, 30.
3 K. Cho, J. Rosmarin and H. Asada, *IEEE Int. Conf. Robot. Autom.*, 2007, 921.
4 E. Smela, *Adv. Mater.*, 2003, **15**, 481.
5 H. Jiang, S. Kelch and A. Lendlein, *Adv. Mater.*, 2006, **18**, 1471.
6 M. Shahinpoor, Y. Bar-Cohen, J. O. Simpson and J. Smith, *Smart Mater. Struct.*, 1998, **7**, R15.
7 H. Yan, K. Tomizawa, H. Ohno and N. Toshima, *Macromol. Mater. Eng.*, 2003, **288**, 578.
8 T. Fukushima, K. Asaka, A. Kosaka and T. Aida, *Angew. Chem., Int. Ed.*, 2005, **44**, 2410.
9 K. Park, M. K. Yoon, S. Lee, J. Choi and M. Thubrikar, *Smart Mater. Struct.*, 2010, **19**, 075002.
10 R. H. Baughman, A. A. Zakhidov and W. A. de Heer, *Science*, 2002, **297**, 787.
11 Y. Zhu, S. Murali, W. Cai, X. Li, J. W. Suk, J. R. Potts and R. S. Ruoff, *Adv. Mater.*, 2010, **22**, 3906.
12 R. H. Baughman, C. Cui, A. A. Zakhidov, Z. Iqbal, J. N. Barisci, G. M. Spinks, G. G. Wallace, A. Mazzoldi,

D. D. Rossi, A. G. Rinzler, O. Jashinski, S. Roth and M. Kertesz, *Science*, 1999, **284**, 1340.
13 K. Mukai, K. Asaka, T. Sugino, K. Kiyohara, I. Takeuchi, N. Terasawa, D. N. Futaba, K. Hata, T. Fukushima and T. Aida, *Adv. Mater.*, 2009, **21**, 1582.
14 D. Li, M. B. Mueller, S. Gilje, R. B. Kaner and G. G. Wallace, *Nat. Nanotechnol.*, 2008, **3**, 101.
15 S. Pei, J. Zhao, J. Du, W. Ren and H. Cheng, *Carbon*, 2010, **48**, 4466.
16 G. W. Rogers and J. Z. Liu, *J. Am. Chem. Soc.*, 2011, **133**, 10858.
17 G. W. Rogers and J. Z. Liu, *J. Am. Chem. Soc.*, 2012, **134**, 1250.
18 X. Xie, L. Qu, C. Zhou, Y. Li, J. Zhu, H. Bai, G. Shi and L. Dai, *ACS Nano*, 2010, **4**, 6050.
19 M. Ghaffari, W. Kinsman, Y. Zhou, S. Murali, Q. Burlingame, M. Lin, R. S. Ruoff and Q. M. Zhang, *Adv. Mater.*, 2013, **25**, 6277.
20 L. Qiu, X. Yang, X. Gou, W. Yang, Z. F. Ma, G. G. Wallace and D. Li, *Chem.–Eur. J.*, 2010, **16**, 10653.
21 L. Lu, J. Liu, Y. Hu, Y. Zhang, H. Randriamahazaka and W. Chen, *Adv. Mater.*, 2012, **24**, 4317.
22 G. Wu, G. H. Li, T. Lan, Y. Hu, Q. W. Li, T. Zhang and W. Chen, *J. Mater. Chem. A*, 2014, **2**, 16836.
23 L. Lu, J. Liu, Y. Hu, Y. Zhang and W. Chen, *Adv. Mater.*, 2013, **25**, 1270.
24 J. Xu, K. Wang, S. Zu, B. Han and Z. Wei, *ACS Nano*, 2010, **4**, 5019.
25 X. Yan, J. Chen, J. Yang, Q. Xue and P. Miele, *ACS Appl. Mater. Interfaces*, 2010, **2**, 2521.
26 G. Wang, W. Xing and S. Zhuo, *Electrochim. Acta*, 2012, **66**, 151.
27 F. Chen, P. Liu and Q. Zhao, *Electrochim. Acta*, 2012, **76**, 62.
28 C. Xu, J. Sun and L. Gao, *J. Mater. Chem.*, 2011, **21**, 11253.
29 J. Zhang and X. S. Zhao, *J. Phys. Chem. C*, 2012, **116**, 5420.
30 S. T. Senthilkumar, R. K. Selvan, N. Ponpandian and J. S. Melo, *RSC Adv.*, 2012, **2**, 8937.
31 C. Meng, C. Liu, L. Chen, C. Hu and S. Fan, *Nano Lett.*, 2010, **10**, 4025.
32 Y. Gao, L. Liu, S. Zu, K. Peng, D. Zhou, B. Han and Z. Zhang, *ACS Nano*, 2011, **5**, 2134.
33 H. Cong, X. Ren, P. Wang and S. Yu, *Energy Environ. Sci.*, 2013, **6**, 1185.
34 S. Ameen, M. S. Akhtar and H. S. Shin, *Sens. Actuators, B*, 2012, **173**, 177.
35 S. H. Domingues, R. V. Salvatierra, M. M. Oliveirab and A. J. G. Zarbin, *Chem. Commun.*, 2011, **47**, 2592.
36 K. Zhang, L. L. Zhang, X. S. Zhao and J. Wu, *Chem. Mater.*, 2010, **22**, 1392.
37 X. Feng, R. Li, Y. Ma, R. Chen, N. Shi, Q. Fan and W. Huang, *Adv. Funct. Mater.*, 2011, **21**, 2989.
38 X. Li, H. Song, Y. Zhang, H. Wang, K. Du, H. Li, Y. Yuan and J. Huang, *Int. J. Electrochem. Sci.*, 2012, **7**, 5163.
39 Z. Q. Niu, L. Zhang, L. Liu, B. W. Zhu, H. B. Dong and X. D. Chen, *Adv. Mater.*, 2013, **25**, 4035.
40 Q. Wu, Y. Xu, Z. Yao, A. Liu and G. Shi, *ACS Nano*, 2010, **4**, 1963.
41 H. L. Wang, J. Gao, J. M. Sanainena and P. MvCarthy, *Chem. Mater.*, 2002, **14**, 2546.
42 O. Kim, T. J. Shin and M. J. Park, *Nat. Commun.*, 2013, **4**, 2208.
43 K. Kaneto, M. Kaneko, Y. Min and A. G. Macdiarmid, *Synth. Met.*, 1995, **71**, 2211.